SPICE-Compatible Equivalent Circuit Models for Accurate Time-Domain Simulations of Passive Photonic Integrated Circuits

Yinghao Ye [iD], *Member, IEEE*, Thijs Ullrick, *Student Member, IEEE*, Wim Bogaerts [iD], *Fellow, IEEE*,
Tom Dhaene [iD], *Senior Member, IEEE*, and Domenico Spina [iD], *Member, IEEE*

Abstract—**Passive photonic integrated circuits (PICs) can be easily characterized in the frequency-domain, but their accurate time-domain performance evaluation is a hurdle for system-level designers, especially when dealing with resonant circuits having highly dispersive behavior, such as ring resonators. In this paper, a new equivalent circuit modeling and simulation approach is proposed, based on the Complex Vector Fitting algorithm, able to perform accurate and robust time-domain simulations of passive PICs directly in standard SPICE simulators. The proposed modeling technique starts from scattering parameters of passive PICs, and is able to capture linear and high order dispersion, backscattering, and wavelength dependent effects. Considering the different nature of optical and electronic signals, a novel concept of equivalent voltage and current for optical waveguides is proposed to simplify the optical to electronic ports conversion and to make it possible to connect and terminate the equivalent circuit models as needed in SPICE simulators, natively supporting bidirectional signal propagation in a waveguide. This work provides a precise and reliable solution to evaluate time-domain characteristics of passive PICs and to access any internal nodes within a circuit, such as the signals inside a ring resonator. Three examples of time-domain simulations of passive PICs in commercial SPICE simulators are presented to demonstrate the flexibility and advantages of the proposed technique.**

Index Terms—**Complex Vector Fitting, photonic integrated circuits, SPICE-compatible equivalent circuits, time-domain simulations.**

I. Introduction

BENEFITING from the combination of a very high index contrast and the compatibility with the CMOS fabrication

technology, silicon photonic integrated circuits (PICs) are experiencing a rapid growth in complexity, functionality, and integration scale. As for electronic integrated circuits (EICs), large and complex PICs design should be circuit-driven, and therefore requires accurate and efficient circuit-level time-domain simulations to reduce design iterations.

However, the lack of a standardized modeling and simulation framework is a significant limiting factor for PICs design. In the field of electronics, circuit simulation of analog EICs has long been standardized with SPICE, later extended by the Verilog-A modeling language. In contrast, the photonics field currently offers several commercial circuit-level simulation tools for PICs, such as Lumerical Interconnect, VPIcomponentMaker Photonic Circuits, Synopsys Optsim, Optiwave's OptiSPICE and IPKISS by Luceda Photonics. Compared to their electronic counterparts, there is no agreement on a standard modelling formalism, let alone a common model definition language [1], [2]. As a result, all these tools have their own model implementations, which are very different from one another. This raises a significant challenge for designers when they need to implement their own models for customized designs or shift to a different commercial simulation tool.

Considering that PICs are comparable to analog EICs, due to the analog nature of photonics, many have proposed to carry out time-domain simulations of PICs in sophisticated electronic simulators based on SPICE or Verilog-A [1], [2], [3], [4], [5], [6]. Literature of the past decades shows many implementations of photonic compact models that are compatible with electronic circuit simulators, such as lasers [7], [8], [9], modulators [10], [11], [12], photodetectors [13], [14], [15], switches [16], etc. For active elements, which contain both electrical and optical ports, this has indeed proven successful, mostly for application cases in optical communications. However, most of these equivalent circuit models for passive PICs have been built by describing their input/output behavior based on analytic models; hence, it can become quite challenging to incorporate wavelength dependent [6] or high-order dispersion [4], [5], especially when propagation is bidirectional and the effects of backscattering or optical return loss need to be included [4], [5], [6]. This could lead to inaccurate simulation results, especially when analyzing large passive PICs consisting of multiple coupling, interference, and/or resonating devices. To the best of our knowledge, even when some works considered back reflections and scattering for

interference-based devices, such as the optical connectors in [3], wavelength dependent effects were not captured.

Another limitation of existing works [2], [3], [4], [5] is the way that signal propagation is implemented. Optical signals are often represented by their complex envelope modulated on a carrier frequency, to eliminate the extremely high-frequency optical oscillations [2], [3], [4], [5], [17]. Typically, optical connections are implemented as a bus of multiple nets, each carrying *either* amplitude/phase or real/imaginary information (since SPICE natively supports only real-valued signals for time-domain analyses) traveling in a *single direction*. As a result, when converting a passive PIC to their equivalent circuit models in SPICE or Verilog-A, the number of ports quadruples: $2\times$ for the two propagation directions and $2\times$ given the complex nature of the signals. In many cases, the number of wires in the bus is furthermore multiplied by the number of modes/polarizations in the waveguide (TE/TM) and the number of wavelength channels. This large number of wires in a bus makes the equivalent circuit models less compact and, as a result, the routing of large systems in schematics can become more confusing [18].

To address these issues, we propose an alternative method to construct accurate SPICE-compatible equivalent circuit models for passive PICs. The modeling process starts from the scattering parameters of the PIC under study, which can be obtained via full-wave electromagnetic simulations. Therefore, high order dispersion, back scattering, and wavelength dependent effects are all properly captured. Then, a corresponding baseband state-space model is computed via the Complex Vector Fitting (CVF) algorithm [17], [19]. This type of model is inherently bi-directional and it can be expressed by a system of real-valued, first-order ordinary differential equations (ODEs), which is well suited to be solved in SPICE simulators. Note that, a software toolbox for the CVF modeling technique has been released in open access [20].

Next, the obtained state-space model is converted into a suitable electrical network, consisting of lumped components and controlled sources. To alleviate the issue of the large increase of input/output ports of the obtained circuit, we introduce the concept of equivalent voltages and currents for optical waveguides, by analogy with microwave circuit theory, which allows for bi-directional propagation of signals on the same wire. As a result, the number of input/output ports in the obtained SPICE-compatible equivalent circuit is only doubled with respect to the actual component, while it is quadrupled for other techniques. Finally, the obtained electrical network (or equivalent circuit) can be simulated in any SPICE-compatible simulation environment, once a suitable simulation set-up is defined by including suitable sources and terminations.

The proposed technique enables fast and accurate time-domain simulation of photonic circuits by leveraging on mature EDA software. Furthermore, by computing an equivalent circuit for each component of a complex PIC and suitably connecting them, designers can perform system level analyses and also access time-domain signals at the connection nodes of different components of a passive PIC. The paper is organized as follows. Section II demonstrates that passive photonic circuits can be modeled with real-valued state-space representations. In Section III, such state-space models are first converted into

SPICE-compatible equivalent circuits, and then forward and backward waves are transformed into voltages and currents, thereby allowing one to cascade the obtained equivalent circuit models in electronic circuit simulators for system simulations. Section IV validates the proposed method by means of three relevant application examples. Conclusions are drawn in Section V.

II. STATE-SPACE MODELS OF PASSIVE PHOTONIC CIRCUITS

Passive photonic circuits can always be characterized by means of the scattering parameters $\boldsymbol{S}$, which are typically obtained via full-wave electromagnetic simulations or transmission measurements (note that this should also include phase measurements, e.g. using an optical vector analyzer). However, due to the high operational frequencies of photonic circuits, it is more computationally efficient to model and simulate the equivalent baseband representation of photonic systems and signals [19], which describes the amplitude and phase envelope of a signal modulated onto an optical carrier frequency. For most applications, these baseband systems and signals are defined at electronic rather than optical frequencies. Additionally, optical signals can always be *analytically* computed starting from their baseband counterpart [19].

In [17], the CVF algorithm was proposed to build state-space models based on the scattering parameters for fast, accurate and robust time-domain simulations of passive photonic circuits. Starting from the baseband scattering parameters $\boldsymbol{S}_{bb}$ of the system under study, evaluated over a discrete set of frequencies over the band of interest for the application at hand, the CVF algorithm [17] is able to build a rational pole-residue model in the form

$$\boldsymbol{S}_{bb}(s) = \sum_{k=0}^{K-1} \frac{\boldsymbol{R}_k}{s - p_k} + \boldsymbol{D} \qquad (1)$$

where $s = j2\pi f$ is the Laplace variable, $\boldsymbol{R}_k$ are the residues, p_k are the poles, which can be either real or complex, and $\boldsymbol{D}$ is a real matrix modeling the asymptotic response at high frequencies. Starting from the rational model in (1) computed via CVF, it is possible to analytically derive the corresponding system of first-order ODEs in the form

$$\begin{cases} \frac{d\boldsymbol{x}(t)}{dt} = \boldsymbol{A}\boldsymbol{x}(t) + \boldsymbol{B}\boldsymbol{a}(t) \\ \boldsymbol{b}(t) = \boldsymbol{C}\boldsymbol{x}(t) + \boldsymbol{D}\boldsymbol{a}(t), \end{cases} \qquad (2)$$

where $\boldsymbol{a}(t) \in \mathbb{C}^{n\times 1}$ and $\boldsymbol{b}(t) \in \mathbb{C}^{n\times 1}$ are the baseband signals which represent incident and outgoing/reflected waves, respectively. $\boldsymbol{x}(t) \in \mathbb{C}^{n\times 1}$ is a state vector, and $\boldsymbol{A} \in \mathbb{C}^{m\times m}$, $\boldsymbol{B} \in \mathbb{R}^{m\times n}$, $\boldsymbol{C} \in \mathbb{C}^{n\times m}$, $\boldsymbol{D} \in \mathbb{R}^{n\times n}$ are state-space parameters, while n is the total number of ports of the system under study and m is the product of n and the number of poles K that are used in the model [17], [20]. Note that, for simplicity reasons, all subscripts that represent baseband signals are omitted in (2) compared to the notation used in [17], [20].

The port signals of the CVF model represented by (2) are complex-valued and describe the amplitude and phase of an signal modulated on the optical carrier wave. Considering the fact that complex numbers are not natively supported by any electronic circuit simulators, a CVF model must be converted

into an equivalent real-valued form before it can be simulated in electronic circuit simulators. In [17] we showed that the real-valued version of a CVF model can be derived by separating the real and imaginary parts of the complex signals and matrices in (2). It has the following form

$$\begin{cases} \frac{d\boldsymbol{x}_\Re(t)}{dt} = \boldsymbol{A}_\Re \boldsymbol{x}_\Re(t) - \boldsymbol{A}_\Im \boldsymbol{x}_\Im(t) + \boldsymbol{B}\boldsymbol{a}_\Re(t) \\ \frac{d\boldsymbol{x}_\Im(t)}{dt} = \boldsymbol{A}_\Re \boldsymbol{x}_\Im(t) + \boldsymbol{A}_\Im \boldsymbol{x}_\Re(t) + \boldsymbol{B}\boldsymbol{a}_\Im(t) \\ \boldsymbol{b}_\Re(t) = \boldsymbol{C}_\Re \boldsymbol{x}_\Re(t) - \boldsymbol{C}_\Im \boldsymbol{x}_\Im(t) + \boldsymbol{D}\boldsymbol{a}_\Re(t) \\ \boldsymbol{b}_\Im(t) = \boldsymbol{C}_\Re \boldsymbol{x}_\Im(t) + \boldsymbol{C}_\Im \boldsymbol{x}_\Re(t) + \boldsymbol{D}\boldsymbol{a}_\Im(t), \end{cases} \quad (3)$$

where the indexes $\Re$ and $\Im$ indicate the real and imaginary parts, respectively. Then, by defining

$$\hat{\boldsymbol{a}}(t) = \begin{bmatrix} \boldsymbol{a}_\Re(t) \\ \boldsymbol{a}_\Im(t) \end{bmatrix}, \ \hat{\boldsymbol{b}}(t) = \begin{bmatrix} \boldsymbol{b}_\Re(t) \\ \boldsymbol{b}_\Im(t) \end{bmatrix}, \ \hat{\boldsymbol{x}}(t) = \begin{bmatrix} \boldsymbol{x}_\Re(t) \\ \boldsymbol{x}_\Im(t) \end{bmatrix} \quad (4)$$

and

$$\hat{\boldsymbol{A}} = \begin{bmatrix} \boldsymbol{A}_\Re & -\boldsymbol{A}_\Im \\ \boldsymbol{A}_\Im & \boldsymbol{A}_\Re \end{bmatrix}, \qquad \hat{\boldsymbol{B}} = \begin{bmatrix} \boldsymbol{B} & \boldsymbol{0} \\ \boldsymbol{0} & \boldsymbol{B} \end{bmatrix},$$

$$\hat{\boldsymbol{C}} = \begin{bmatrix} \boldsymbol{C}_\Re & -\boldsymbol{C}_\Im \\ \boldsymbol{C}_\Im & \boldsymbol{C}_\Re \end{bmatrix}, \qquad \hat{\boldsymbol{D}} = \begin{bmatrix} \boldsymbol{D} & \boldsymbol{0} \\ \boldsymbol{0} & \boldsymbol{D} \end{bmatrix}, \quad (5)$$

where $\boldsymbol{0}$ represents the null matrix, (3) can be written as [17]

$$\begin{cases} \frac{d\hat{\boldsymbol{x}}(t)}{dt} = \hat{\boldsymbol{A}}\hat{\boldsymbol{x}}(t) + \hat{\boldsymbol{B}}\hat{\boldsymbol{a}}(t) \\ \hat{\boldsymbol{b}}(t) = \hat{\boldsymbol{C}}\hat{\boldsymbol{x}}(t) + \hat{\boldsymbol{D}}\hat{\boldsymbol{a}}(t). \end{cases} \quad (6)$$

It is important to remark that it is possible to guarantee the stability and passivity of CVF models in the form (6). In particular, stability can be guaranteed by construction, while passivity can be checked (and enforced if needed) as a post-processing step [17]. Note that, a publicly available MATLAB implementation of the CVF algorithm is available at http://sumo.intec.ugent.be/CVF, including routines for passivity assessment and enforcement of CVF models. Giving a detailed description of the CVF modeling method is outside of the scope of this contribution, the interested reader is referred to [17], [20] for a complete discussion on the properties of the CVF technique. It is worth mentioning that the real/imaginary form is used in this work as opposed to magnitude/phase form, since the latter one could create some problems as mentioned in [4], [21].

Now, passive photonic circuits can be represented by real-valued state-space models in the form of (6), which is suitable to be simulated in SPICE simulators (where only real numbers are supported). In next section, a method is presented to convert this real-valued mathematical model to a SPICE-compatible equivalent circuit model.

III. SPICE-COMPATIBLE EQUIVALENT CIRCUIT MODELS FOR PASSIVE PHOTONIC CIRCUITS

A. Converting State-Space Models into Electronic Circuits

Mathematically, the real-valued model represented by (6) consists of a set of first-order linear differential equations, which, in principle, can be solved by SPICE. To do so, (6) needs to be converted into a SPICE netlist consisting of elementary electronic circuit elements.
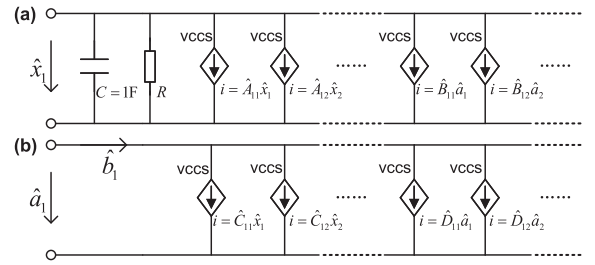

Fig. 1. SPICE-compatible equivalent circuit diagram for real-valued state-space models of passive photonic circuits. (a) equivalent circuit of the first differential equation in the real-valued model; (b) equivalent circuit of the first linear equation in the real-valued model.
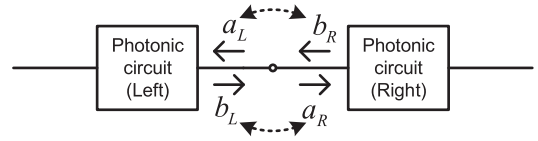

Fig. 2. Relations of optical signals at the node of two connected photonic circuits.

It can be observed that such real-valued model contains three mathematical operations: differentiation, addition, and multiplication. The set of linear differential equations can be modeled with an array of capacitors interconnected by voltage controlled current sources [22]. Meanwhile, the state variables $\hat{\boldsymbol{x}}(t)$ and incident waves $\hat{\boldsymbol{a}}(t)$ are numerically mapped to voltage signals in SPICE, as shown in Fig. 1(a). A very large resistor R (e.g. $> 10^{18}\Omega$) is added to prevent floating nodes and will not affect the behavior of the circuit [22]. Similar implementations of ordinary differential equations in other fields can be found in [23], [24]. Then, following Kirchhoff's current law, the set of linear equations for the reflected waves $\hat{\boldsymbol{b}}(t)$ can be converted into multiple parallel branches containing voltage controlled current sources [25], where the backward waves are interpreted as the total current of all parallel branches, as shown in Fig. 1(b). Note that the time dependency of $\hat{\boldsymbol{x}}(t)$, $\hat{\boldsymbol{a}}(t)$, and $\hat{\boldsymbol{b}}(t)$ is omitted in Fig. 1, for simplicity.

Now, given the forward waves $\hat{\boldsymbol{a}}(t)$, the backward waves $\hat{\boldsymbol{b}}(t)$ can be obtained via simulating this equivalent circuit model in any SPICE simulator. However, this is only suitable for simulating a standalone passive photonic device or circuit. Indeed, problems will appear when connecting ports of these models. For example, let us assume that two passive photonic circuits with two input/output ports are physically connected with the same waveguide cross section (the propagation constants and mode profiles at the interface are matched): the waves (b_R or b_L) emanating from the circuit on one side of a reference plane equal to the waves (a_L or a_R) entering the circuit on the other side of the reference plane, as depicted in Fig. 2. Due to the fact that incident and reflected waves are mapped to voltages and currents in the equivalent SPICE model shown in Fig. 1, respectively, SPICE simulators will assume $a_L = a_R$ and $b_R = -b_L$ when the SPICE models of these two photonic circuits are directly cascaded, which is obviously wrong. This is because voltage and current are signals of conservation systems that are formulated using conservation laws at the connection nodes, and comply

with KCL and KVL. In contrast, forward and backward optical waves are intrinsically traveling electromagnetic waves and they follow signal-flow-graph theory in this scenario.

To solve this problem, in next section we introduce the concept of equivalent voltage and current for optical waveguides by analogy in microwave circuit theory.

B. Equivalent Voltages and Currents of Optical Waveguides

At low frequencies, electronic circuits that contain lumped elements are described and analyzed with voltages and currents. At high frequencies, microwave circuits that contain distributed elements are characterized with electric and magnetic fields. In order to facilitate the analysis of microwave circuits, equivalent voltages and currents of waveguides were proposed to make optimum use of low frequency circuit concepts, which serves as a cornerstone of microwave circuit theory (or waveguide circuit theory) [26]. This brings great advantages, since it makes it possible to analyze waveguide-based systems with conventional circuit theory and simulate microwave circuits in SPICE simulators.

Passive photonic circuits are similar to microwave circuits given that both of them are waveguide-based systems and manipulate the propagation of electromagnetic waves. A main distinction is that photonic circuits deal with optical waves whose frequencies are significantly higher than microwaves. In order to simulate photonic circuits in conventional electronic circuit simulators and to solve the problem mentioned in the previous section, it is necessary to construct the concept of equivalent voltages and currents for optical waveguides, just like it has been done for microwave waveguides.

The total electric and magnetic fields in a single mode of an optical waveguide are combinations of forward and backward propagating mode fields. Therefore, their transverse components can be expressed as

$$\boldsymbol{E}_t = C^+ \boldsymbol{e}_t e^{-j\beta z} + C^- \boldsymbol{e}_t e^{j\beta z},$$
$$\boldsymbol{H}_t = C^+ \boldsymbol{h}_t e^{-j\beta z} - C^- \boldsymbol{h}_t e^{j\beta z}. \qquad (7)$$

In (7), C^+ and C^- are arbitrary amplitude constants, β is the propagation constant, $\boldsymbol{e}_t$ and $\boldsymbol{h}_t$ are the transverse components of electric and magnetic fields, respectively, which are related to each other by $\boldsymbol{h}_t = (\boldsymbol{z} \times \boldsymbol{e}_t)/Z_w$ and Z_w is the wave impedance. Only transverse fields are taken into account since axial components do not contribute energy at the terminal plane of each waveguide port, as described by (9).

By exploring the microwave circuit theory [26], the equivalent voltage and current are defined as:

$$V = V^+ + V^- = K_1 C^+ e^{-j\beta z} + K_1 C^- e^{j\beta z},$$
$$I = I^+ - I^- = K_2 C^+ e^{-j\beta z} - K_2 C^- e^{j\beta z}, \qquad (8)$$

where $V^+ = K_1 C^+ e^{-j\beta z}$, $V^- = K_1 C^- e^{j\beta z}$, and $I^+ = K_2 C^+ e^{-j\beta z}$, $I^- = K_2 C^- e^{j\beta z}$. V^+ and I^+ can be considered as forward propagating voltage and current waves, respectively, while V^- and I^- are the backward propagating ones. Note that K_1 and K_2 are constants of proportionality introduced to conserve power that are calculated from equivalent voltage, current and transverse electric and magnetic fields, as shown below

$$\frac{1}{2}V^+(I^+)^* = \frac{|C^+|^2}{2}\int_S \boldsymbol{e}_t \times \boldsymbol{h}_t^* \cdot \boldsymbol{z} dS, \qquad (9)$$

which can be simplified to

$$K_1 K_2^* = \int_S \boldsymbol{e}_t \times \boldsymbol{h}_t^* \cdot \boldsymbol{z} dS. \qquad (10)$$

(9) calculates the total complex power over the cross section S of a waveguide, which imposes a constraint on K_1 and K_2. As pointed out in [26], $K_1 K_2^*$ can be forced to unity by proper normalization of $\boldsymbol{e}_t$ and $\boldsymbol{h}_t$. Then, the forward a and backward b waves that define the scattering parameters can be represented by $C^+ e^{-j\beta z}$ and $C^- e^{j\beta z}$, respectively, and there is

$$V^+(I^+)^* = aa^*, \quad V^-(I^-)^* = bb^*. \qquad (11)$$

To determine K_1 and K_2, a second constraint is required:

$$Z = \frac{V^+}{I^+} = \frac{V^-}{I^-} = \frac{K_1}{K_2}. \qquad (12)$$

The ratio Z between K_1 and K_2 can be considered as equivalent characteristic impedance. Now, the net power into each port can be calculated as

$$P = \frac{|a|^2 - |b|^2}{2} = \frac{V^+(I^+)^* - V^-(I^-)^*}{2} = \frac{\Re(VI^*Z^*)}{2Z^*}. \qquad (13)$$

(13) demonstrates that only when Z is chosen to be real, the net power calculated from V and I is equal to the difference between the powers carried by the forward and backward waves. With a real-valued Z, port voltages and currents can be represented by linear combinations of forward and backward waves via simple manipulation of (8), (11), and (12)

$$V = V^+ + V^- = \sqrt{Z}(a + b),$$
$$I = I^+ - I^- = \frac{a - b}{\sqrt{Z}}. \qquad (14)$$

and $V^+ = \sqrt{Z}a, V^- = \sqrt{Z}b, I^+ = a/\sqrt{Z}, I^- = b/\sqrt{Z}$.

C. Connection and Termination of SPICE Equivalent Circuit Models

Section III-A mentioned that SPICE-compatible circuit models (in Fig. 1) of passive photonic devices can not be directly cascaded in circuit simulators. Using the novel definition of equivalent voltage and current for optical waveguides as derived in Section III-B, the ports represented by $\hat{\boldsymbol{a}}(t)$ and $\hat{\boldsymbol{b}}(t)$ in Fig. 1 can be converted into ports represented by voltages and currents. To do so, first (14) is written as

$$a = \frac{V + ZI}{2\sqrt{Z}},$$
$$V = ZI + 2\sqrt{Z}b. \qquad (15)$$

The first equation of (15), converting the incident wave a, corresponding to the port voltage of the SPICE-compatible circuit in Fig. 1, to the equivalent voltage and current, is implemented by the series connection of a voltage controlled voltage source with amplitude $\frac{V}{2\sqrt{Z}}$ and a current controlled voltage
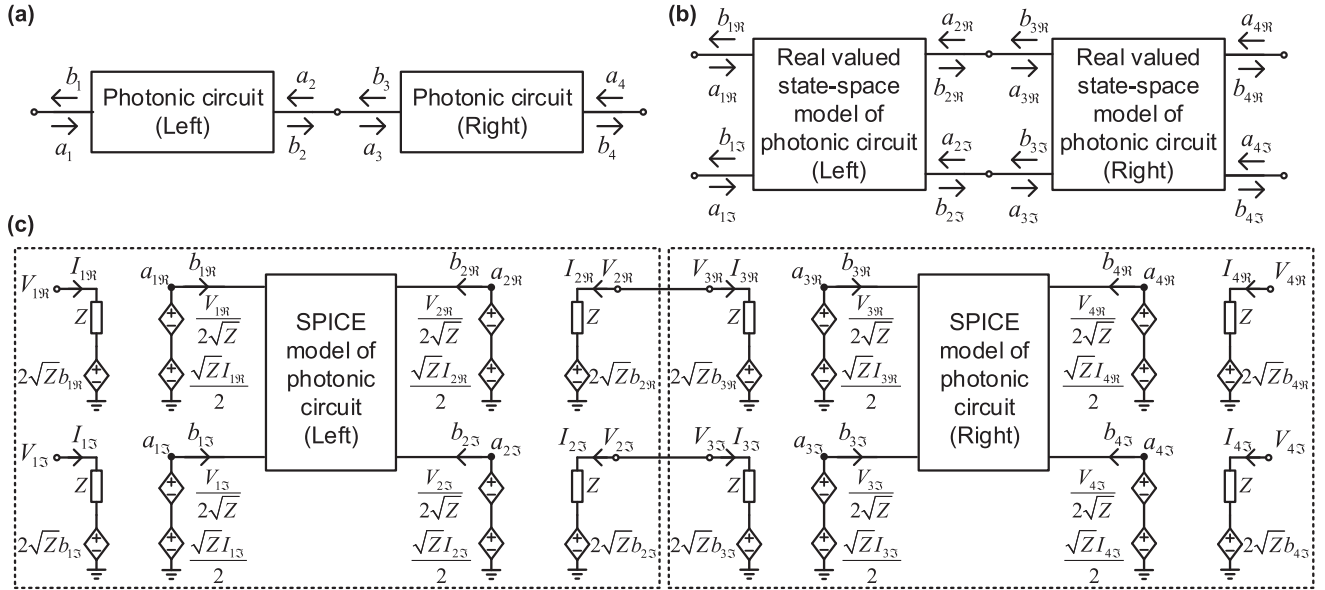
(a)

(b)

(c)

Fig. 3.   Connection of SPICE equivalent circuit models for passive photonic circuits. (a) cascading of two two-port photonic circuits; (b) connection of the corresponding real-valued state-space models represented by (6); (c) connection of the corresponding SPICE equivalent circuit models illustrated in Fig. 1.

source with amplitude $\frac{ZI}{2\sqrt{Z}}$. Similarly, the second equation of (15), relating the equivalent voltage to the equivalent current and reflected wave b, corresponding to the port current of the SPICE-compatible circuit in Fig. 1, is implemented by a current controlled voltage source with a series resistance Z. The result of adding these external components is that the photonic scattering waves are mapped to equivalent voltage and current signals that allow to cascade SPICE-compatible circuits while respecting the underlying physics.

To better illustrate this idea, an example of cascading the SPICE models of two photonic circuits with two input/output ports is presented in Fig. 3. It can be observed from Fig. 3(a) and (b) that one physical port of a photonic circuit corresponds to two ports of a real-valued state-space model, as explained in Section II. Fig. 3(c) demonstrates how to implement the interface conversion through (15) and how to cascade two SPICE equivalent circuit models after the interface conversion.

Now, let us consider one node in Fig. 3(b), for example the one where $a_{2\Re} = b_{3\Re}$ and $b_{2\Re} = a_{3\Re}$. According to (14), the relations $V_{2\Re} = V_{3\Re}$ and $I_{2\Re} = -I_{3\Re}$ can be easily derived, which suggests that $V_{2\Re}$, $V_{3\Re}$, $I_{2\Re}$, and $I_{3\Re}$ at the corresponding node in Fig. 3(c) comply with KVL and KCL. Note that, while Fig. 3 presents a series connection of two photonic circuits, this method can be immediately generalized to large photonic circuit networks that are connected in an arbitrarily complex manner.

It is important to remark that, when physically cascading multiple photonic circuits in real life designs, pairs of identical waveguides (or ports) are joined without discontinuity. Therefore, in this work, only nodes that link two waveguides (or ports) are considered, whereas any junctions connecting three or more waveguides (or ports), such as splitters, should be treated as passive devices with their own internal SPICE circuit.

When it comes to simulating the SPICE circuit model in Fig. 3(c), another practical issue is how to excite it with a given incident wave and how to terminate the circuit's ports. Let us
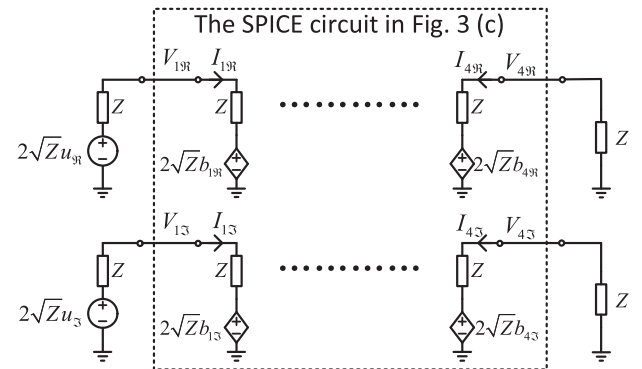

Fig. 4.   Termination of SPICE equivalent circuit models for time-domain simulations when port 1 of the circuit in Fig. 3(a) is excited and port 4 is unused.

assume that port 1 in Fig. 3(a) is excited by an optical wave u which is a complex-valued time-dependent signal. The time dependency is omitted for u to keep it consistent with the notation used in Fig. 3. Hence, the incident wave a_1 at port 1 equals u which for the real-valued model in Fig. 3(b) becomes $a_{1\Re} = u_\Re$, $a_{1\Im} = u_\Im$, with $u_\Re$ and $u_\Im$ the real and imaginary parts of u, respectively. Accordingly, two sources should be properly attached to the ports represented by $(V_{1\Re}, I_{1\Re})$ and $(V_{1\Im}, I_{1\Im})$ in Fig. 3(c). This can be implemented by connecting a Thevenin voltage source with output resistance Z to an external port of the SPICE circuit, as shown in Fig. 4. The signal amplitude of Thevenin voltage driver must satisfy

$$V_{1\Re} = 2\sqrt{Z}u_\Re - ZI_{1\Re} = \sqrt{Z}(u_\Re + b_{1\Re}),$$

$$V_{1\Im} = 2\sqrt{Z}u_\Im - ZI_{1\Im} = \sqrt{Z}(u_\Im + b_{1\Im}). \qquad (16)$$

Any open ports that are not connected to other circuits must be carefully terminated with a matched resistor Z to prevent back reflections. Doing this, only the backward wave b will emanate

from the port while the incident wave a disappears. This leads to

$$V_{4\Re} = \sqrt{Z}b_{4\Re}, \quad I_{4\Re} = -b_{4\Re}/\sqrt{Z},$$

$$V_{4\Im} = \sqrt{Z}b_{4\Im}, \quad I_{4\Im} = -b_{4\Im}/\sqrt{Z}, \quad (17)$$

Supposing the ports represented by $(V_{4\Re}, I_{4\Re})$ and $(V_{4\Im}, I_{4\Im})$ in Fig. 3(c) are not connected to any source when performing time-domain characterization, this means they thus must be properly terminated by matched resistor Z, as is shown in the simulation set-up depicted in Fig. 4.

It is important to remark that the value of the equivalent characteristic impedance Z can be chosen arbitrarily when computing an equivalent circuit of a passive photonic device via the proposed method. However, when connecting the obtained equivalent circuit with others computed with the same approach, it is important that the characteristic impedance adopted is the same for all circuits. Otherwise, a mismatch will be introduced at the connecting nodes of any two circuits, due to the different mapping adopted when converting optical waves into voltages and currents, and the accuracy of the corresponding simulation results will decrease. Note that a similar condition holds in the microwave domain: in order to connect systems described by their scattering parameter representations, it is necessary that the value of the reference impedance used to compute the scattering matrix is the same for all systems under study. Additional details are given in the next section, along with the definition of the reference impedance.

D. Equivalent Circuits for Photonic and Electronic Devices

It is important to remark that equations (14)–(17) derived above are equivalent to the corresponding equations for microwave components. The main difference resides in the definition of the impedance Z. For microwaves electronic circuits, Z corresponds to the characteristic impedance of the transmission lines used to measure (or simulate) the scattering parameters: as such, it is also called *reference impedance*. Hence, the value of the scattering parameters depends on the specific reference impedance chosen during measurements or simulations [27]. This does not hold for the characteristic impedance Z defined in Section III-B, which is introduced only to obtain a consistent mapping between photonic waves and voltages and currents and does not have any influence on the computation of the scattering matrix of the photonic system under study.

However, given that the mapping of optical waves into electrical signals presented here is consistent with the corresponding one defined in the microwave domain, in principle it is possible to adopt any technique presented in the microwave domain to convert real-valued state-space models of scattering parameters into SPICE-compatible equivalent circuits, in order to compute the desired equivalent circuit for any passive photonic device, as long as the conversion from waves into electrical signals is defined as described in Section III.

For example, the technique [25] adopts a similar approach to the one described in the previous sections, based on controlled sources and the reference impedance, to convert microwave incident and reflected waves into voltages and currents. By substituting the reference impedance with the characteristic
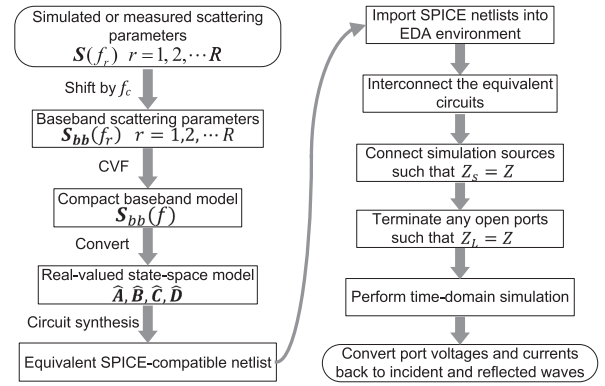

Fig. 5. Flowchart of the proposed modeling and simulation method; Z_S is the output impedance of the simulation source, Z_L represents the external resistance used to terminate open ports and Z is the characteristic impedance used to compute the equivalent circuit.

impedance Z defined in Section III-B and by choosing excitation and terminations as described in Section III-C, it is possible to use the technique [25] to derive and simulate an equivalent SPICE-compatible circuits for passive photonic components.

The flowchart of the proposed modeling and simulation method is illustrated in Fig. 5.

IV. NUMERICAL EXAMPLE

This section presents three application examples of the proposed technique. In order to show the flexibility of the proposed approach, two different circuit simulators will be used: LTspice of Analog Devices and Advanced Design System (ADS) of Keysight Technologies. In order to prove that the value of the characteristic impedance Z can be freely chosen, the value $Z = 50\ \Omega$ will be used in the first application example, while $Z = 1\ \Omega$ will be adopted for the examples in Sections IV-B and IV-C.

The CVF modeling algorithm starts from the baseband scattering parameters of the system under study. Hence, the obtained equivalent netlist is only valid for one optical carrier frequency, corresponding to the baseband shift of the scattering parameters. Time-domain simulation of multiple wavelength channels requires the computation of a new CVF model and corresponding equivalent netlist for each optical carrier propagating in the system. However, in the three numerical examples presented in this work, only single wavelength signals are considered.

A. Mach-Zehnder Interferometer

In this first example, an ideal *Mach-Zehnder interferometer* (MZI) is studied, which is composed by two *directional couplers* (DCs) and two waveguides, as shown in Fig. 6. For this example, the scattering parameters of the MZI are analytically defined and do not take into account back-reflections, scattering and wavelength dispersion. This simple example allows us to clearly illustrate the characteristics of the proposed approach and to validate the obtained results against analytical calculations.

By focusing on the analytic expressions of the transfer function corresponding to the bar (S_{13}) and cross port (S_{14}) of the device in a sparse matrix, a frequency domain model can
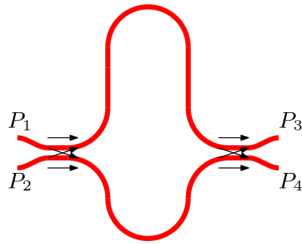
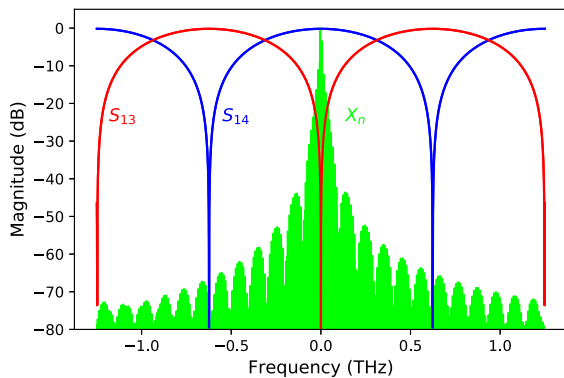Fig. 6.   The structure of the Mach-Zehnder interferometer under study.

Fig. 7.   The normalized DFT spectrum X_n of the 4-QAM input signal (green line) plotted along the baseband analytical scattering parameters of the ideal MZI (red and blue lines).

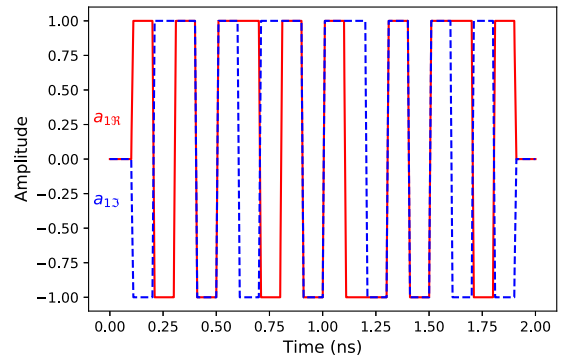
Fig. 8.   The in-phase part (red) and quadrature part (blue) of the 10 Gbit/s and 12 bits long 4-QAM input signal applied to P1 of the MZI.

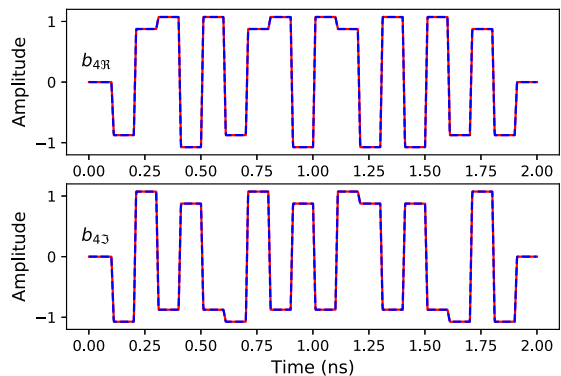
Fig. 9.   Time-domain SPICE simulation of the MZI output at $P4$ (red) compared to the analytical output response (blue).

be constructed for evaluation of the scattering parameters. The transfer function of the bar and cross port can be written as [28]

$$S_{13}(\omega) = \sqrt{r_1 r_2} e^{-j\omega \Delta t_1} - \sqrt{(1-r_1)(1-r_2)} e^{-j\omega \Delta t_2}$$
$$S_{14}(\omega) = j\sqrt{(r_1(1-r_2))} e^{-j\omega \Delta t_1} + j\sqrt{(1-r_1)r_2} e^{-j\omega \Delta t_2}$$
(18)

with r_1 and r_2 the self-coupling coefficients of the directional couplers and Δt_1 and Δt_2 the delays in the upper and lower arm, respectively. In this example, r_1 and r_2 are selected for a 50:50 symmetrical directional coupler with 2% power losses, $\Delta t_1 = 0.4\,\text{ps}$ and $\Delta t_2 = 1.2\,\text{ps}$. The time-domain output response corresponding to the scattering matrix definition of (18) can be analytically derived and results from the two-beam interference of the signals propagating in the upper and lower arm of the MZI. Time-domain simulation of the analytical model is implemented in the Caphe circuit simulator of Luceda Photonics.

The analytically defined scattering parameters of the device, shown in Fig. 7, are evaluated in the frequency range $[192.17; 194.67]$ THz (corresponding to a wavelength range of $[1.54; 1.56]$ μm) while considering a carrier frequency $f_c = 193.46$ THz $(1.55\,\mu\text{m})$. In this example, 81 frequency samples are used, and they are uniformly distributed over the frequency range of interest. Following the CVF modeling procedure, a stable and passive CVF model is built with 6 poles, leading to a maximum modeling error between the data and the model's response below $-47\,\text{dB}$. Then, the real-valued state-space model (6) is computed and converted into an electrical circuit as described in Section III. The characteristic impedance used to generate the circuit is set to $50\,\Omega$. Finally, the SPICE

netlist is imported in ADS, simulation sources are connected and any remaining open ports are properly terminated.

In particular, the MZI is simulated in ADS by applying an ideal 4 quadrature amplitude modulation (QAM) input signal at port $P1$ (no noise or overshoot/undershoot present on the signal). The in-phase and quadrature component of $P1$ are each excited by an RF bit sequence with bit rate 10 Gbit/s and 12 bits long. The bit sequence and its baseband DFT spectrum $(I(f) + jQ(f))$ are shown in Figs. 8 and 7, respectively. A time-domain simulation of the MZI circuit is performed in ADS and the output response at the cross port is compared to the corresponding value obtained via the analytical time-domain model. As it can be observed in Fig. 9, the time-domain SPICE simulation of the MZI shows very good convergence with respect to the one obtained by directly using the analytical model. Fig. 10 illustrates the amplitude error of the SPICE simulation with respect to the analytical response at each time step. While the absolute error is usually well below 10^{-3}, it increases around sharp signal transitions. This is caused by numerical effects that are more prominent for sharp signal transitions, which have high-frequency components, and this also depends on the finite time step used to simulate the circuit, the modeling error associated with the CVF model and the technique used to solve the Modified Nodal Analysis (MNA) matrix in the circuit simulator.

To illustrate that port terminations must be matched to the characteristic impedance Z used to compute the equivalent circuit, we conduct the following experiment: time-domain simulations of the MZI circuit are performed for several values of
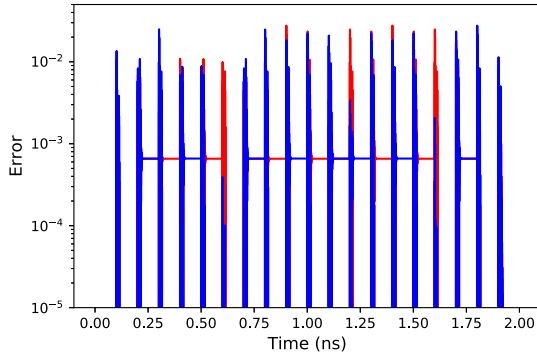
Fig. 10. Amplitude of the error between the SPICE and analytical output response; the red solid line represents the error corresponding to $b_{4\Re}$ while the blue solid line represents the error of $b_{4\Im}$.
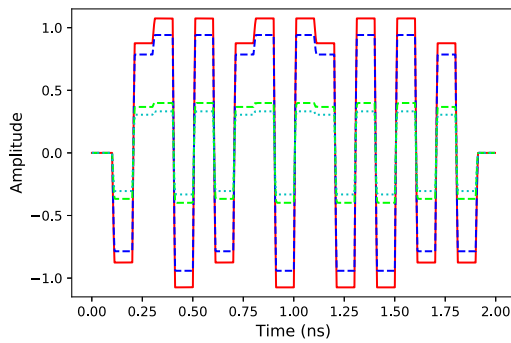

Fig. 11. Transient output response of the signal $b_{4\Re}$ corresponding to the ideal $50\,\Omega$ MZI circuit; the simulation is repeated for external resistance values of $10\,\Omega$ (lime), $30\,\Omega$ (blue) and $200\,\Omega$ (cyan); the solid red line represents the analytical output response.

the port resistances, different from the value $Z = 50\,\Omega$ used to compute the equivalent circuit. Fig. 11 shows that as the impedance mismatch becomes larger, the distortion of the output response increases as well. This can be understood by noting that as the impedance mismatch becomes larger, more power is reflected back towards the load. Since these reflections are non-inherent to the operating conditions of the MZI, they act as parasitics and distort the output response. Therefore, it is fundamental to match all port terminations to the reference impedance of the circuit when conducting SPICE simulations.

B. Ring Resonator Filter

In this section, a five-ring resonator filter that comprises four DCs and two multimode interferometers (MMIs) will be studied. The CVF model of this filter was built and simulated in MATLAB in a previous work [17]. In this paper, the corresponding SPICE equivalent circuit model will be built with the proposed technique and then simulated in LTspice. Since the results obtained from time-domain simulation of the CVF models in MATLAB are verified in [17], [19], [20], [29], they will serve as a benchmark in this work to evaluate the accuracy of the proposed technique.

The structure of the filter is shown in Fig. 12. The scattering matrices of this filter are obtained by the method mentioned in [17] and the frequency response is plotted in Fig. 13. Interested readers are referred to [17] for more detailed information about
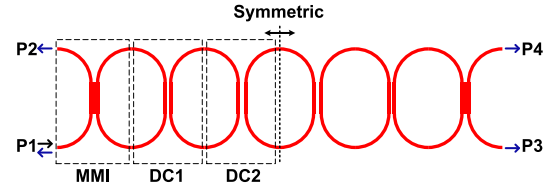

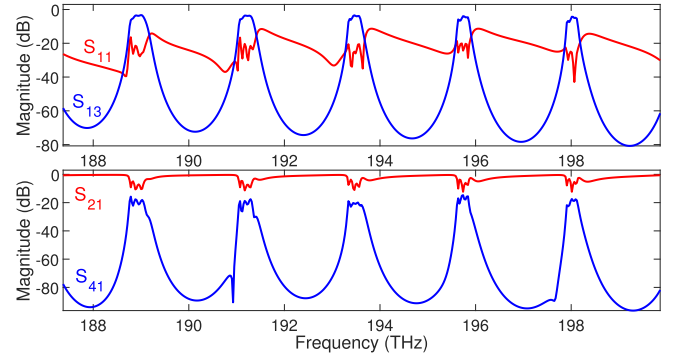Fig. 12. The geometric structure of the five-ring resonator filter.

Fig. 13. The frequency responses of the five-ring resonator filter.

this filter. The modeling process starts with the CVF model of the filter in the form (2), which is built upon the frequency range $[187.37; 199.86]$ THz (corresponding to a wavelength of $[1.5; 1.6]\,\mu m$), while considering a carrier frequency $f_c = 193.46$ THz. Then, a real-valued model can be immediately derived according to Section II. Finally, a SPICE equivalent circuit model in the form shown in Fig. 3(c) is constructed from the real-valued model via the approach proposed in Section III. Note that the resulting circuit model is generated in the form of a netlist.

Let us assume that port 1 of the filter is excited by an amplitude modulated optical signal with carrier frequency $f_c = 193.46$ THz, while all other ports are properly terminated to avoid reflections, and the amplitude modulating signal is a narrow pulse with a width of 1 ps and spectrum in the range $[0; 6]$ THz. Note that, in practice, it is difficult to generate a pulse with such narrow width of 1 ps: this extreme situation is intentionally applied to impose more challenges on the time-domain simulation, thereby demonstrating the capability of the proposed method. Since a baseband equivalent signal of an amplitude modulated signal is purely real [29], there are $u(t) = u_{\Re}(t) = a_{1\Re}(t)$ and $u_{\Im}(t) = a_{1\Im}(t) = 0$. Then, the obtained equivalent circuit model is excited and terminated in LTspice in the way illustrated by Fig. 4 to perform time-domain simulations. Meanwhile, the CVF model of the filter is simulated in MATLAB for comparison. It is worth mentioning that, depending on the organization of the SPICE code, if only the port voltage and current in Fig. 4 are accessible after SPICE simulations, one more step is required to calculate the forward and backward waves according to (14).

Fig. 14 shows the real and imaginary parts of the incident wave at port $P1$ that excites the CVF model. After carrying out the simulation of the corresponding SPICE model, incident waves are recovered from the voltage and current at port $P1$ according to (14) and are also depicted in Fig. 14 for comparison,
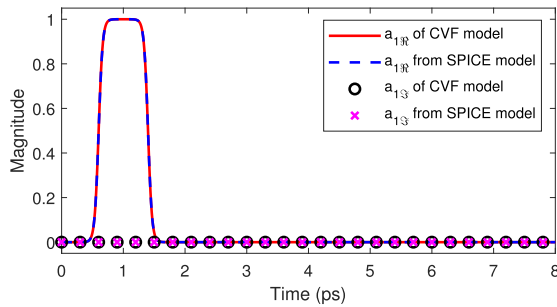
Fig. 14.   The forward wave (excitation signal) recovered from the voltage and current at port $P1$ of the SPICE equivalent circuit.
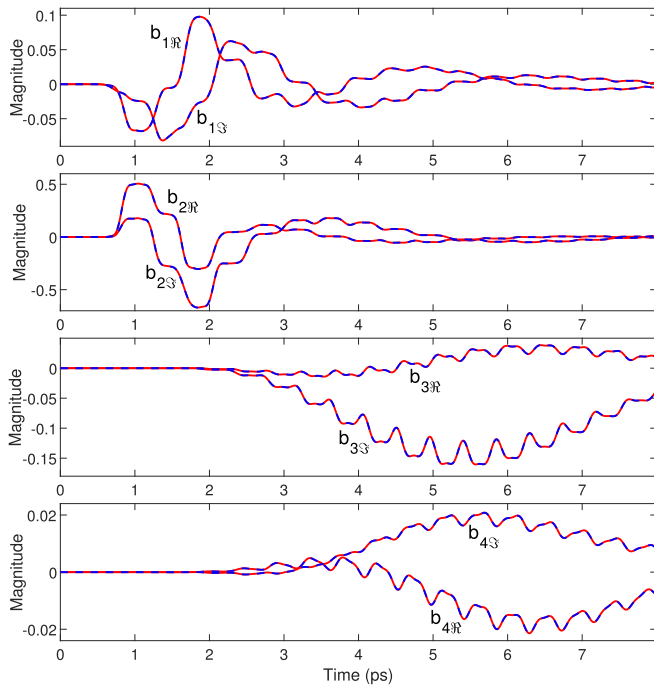

Fig. 15.   The outputs (backward waves) at each port of the five-ring filter. The red lines represent the simulation results of the CVF model while the blue dash lines represent that of the SPICE model.
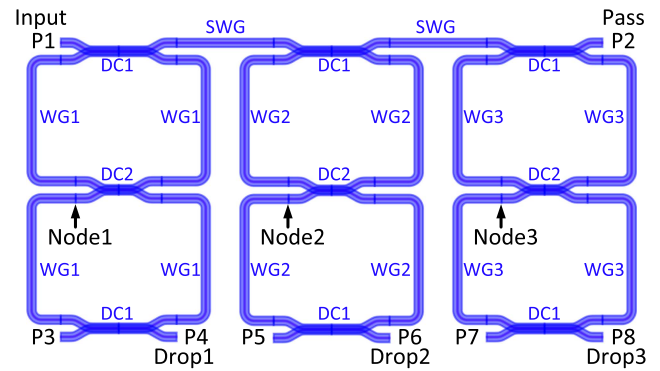

Fig. 16.   Layout of the three-stage double-ring WDM filter.

excitation port and the delays between the excitation signal and the outputs.

In terms of simulation efficiency, the CVF model takes 0.2 s in MATLAB, while the SPICE model requires 2.9 s in LTspice. These computational times have been obtained with a personal computer with Intel Core i5 processor and 8 GB RAM. The simulation in SPICE is less efficient, as it is a modified nodal solver rather than a numerical differential equation solver. It means that, at every time step the SPICE solver needs to first transform the energy-storage components (capacitors in this scenario) into their linear companion models and then convert the netlist into new nodal matrices according to KCL, before solving the linear nodal equations [30]. The *lsim* solver in MATLAB adopts the state propagation method, which is even faster than ordinary differential solvers, since it first discretizes the continuous-time state-space model and then conducts only two matrix-vector products, namely the state transition matrix times the state vector and the input matrix times the input vector for each time step [31].

C. Wavelength-Division Multiplexing Filter

In this numerical example we consider the case of a wavelength-division multiplexing (WDM) filter, implemented by a cascaded combination of three stages of double ring resonators loaded on a common bus waveguide, as illustrated in Fig. 16. This type of filter is usually used to separate the RF channels modulated on different optical carriers. The channel spacing in this application example is 35 GHz at a center frequency of 193.42 THz ($1.55\,\mu m$) and each channel is chosen to have a bandwidth of 35 GHz. In this section, we will evaluate the time-domain crosstalk between adjacent channels with given input signals via the proposed technique. Remark that such a characterization is a crucial step in signal integrity analysis. Additionally, we will demonstrate that the proposed technique enables us to access signals at any internal node of a photonic circuit (e.g. signals inside the ring resonators of the WDM filter). The WDM filter consists of nine S-bend DCs and fourteen waveguides (WGs) in total, as shown in Fig. 16. To achieve the desired bandwidth and channel spacing, the coupling coefficients of the S-bend DCs in the layout are tuned by varying the length of their coupling region and the lengths

which demonstrates that the excitation circuit in Fig. 4 has the same effect of directly exciting port $P1$ of the filter with the incident wave. Furthermore, all the output signals (backward waves in this case) are immediately obtained via simulating the CVF model with *lsim* in MATLAB and the SPICE model with LTspice. Note that the MATLAB routine *lsim* allows us to integrate systems of ordinary differential equations. Fig. 15 presents the simulation results. It can be observed that the results from both simulations show excellent agreement, and the maximum absolute error among the two simulation methods is less than 5.11×10^{-4}, and thus not plotted in Fig. 15. Due to the fact that the passband of the filter is very narrow compared with the spectrum of the excitation signal, as shown in Fig. 13, the output signals at ports $P3$ and $P4$ are quite weak while the transmission at port $P2$ is much stronger. Furthermore, it is possible to clearly observe the strong back reflection at the

Fig. 17. Transmission spectrum corresponding to the three drop ports of the WDM filter.

Fig. 18. SPICE equivalent circuit representations of the WDM filter in Fig. 16. (a) Single SPICE equivalent circuit model representing the S-matrix of the entire filter. (b) Hierarchical connection of the SPICE equivalent subcircuits corresponding to the 9 DCs and 14 WGs forming the WDM filter.

Fig. 19. The in-phase part (red) and quadrature part (blue) of the 16 QAM excitation signal.

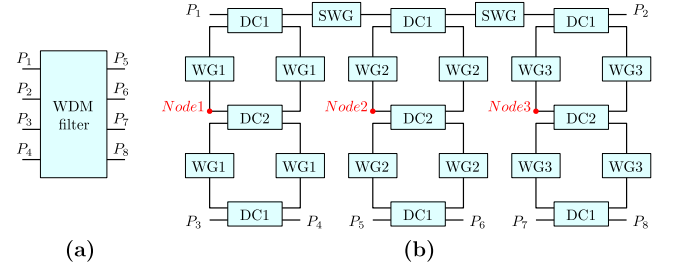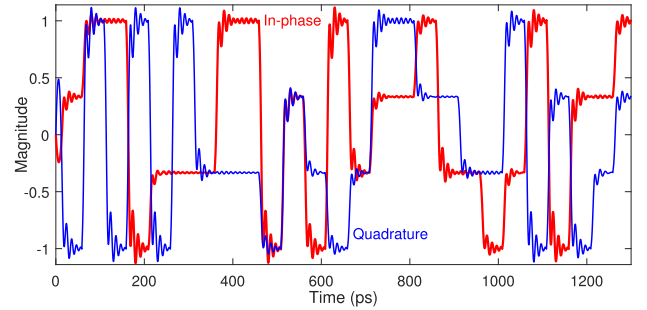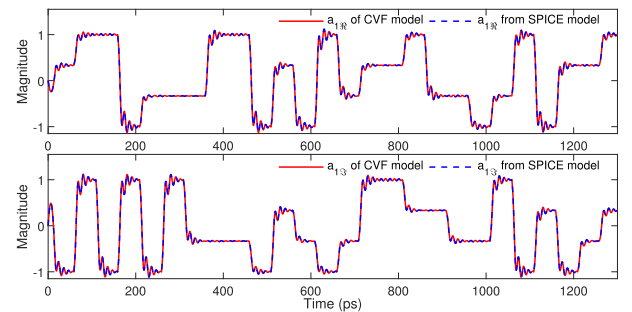Fig. 20. The forward wave (excitation signal) recovered from the port voltage and current at $P1$ of the SPICE equivalent circuit model of the WDM filter.

of the waveguides in each ring are also carefully chosen. By simulating in Lumerical FDTD, DC1 and DC2 in Fig. 16 are tuned to have a power coupling of $\kappa_1 = 0.52$ and $\kappa_2 = 0.14$, respectively. On the other hand, the waveguides are modeled by their effective index $n_{eff} = 2.27$, group index $n_g = 4.54$ and losses $\alpha = 1.91$ dB/cm. The round trip lengths of the rings are the same within a single stage, and they are designed to match the specified passbands while guaranteeing a free spectral range (FSR) greater than 210 GHz. The scattering matrices of the DCs are extracted from Lumerical FDTD simulations, while those of the WGs are computed in Luceda IPKISS. For ease of reference, all ports of the WDM filter are annotated from $P1$ to $P8$, while the internal nodes of interest are marked as Node1 to Node3. The transmission from input $P1$ to the three drop ports ($P4$, $P6$, and $P8$) is plotted in Fig. 17.

The filter is excited at $P1$ with a 16-QAM signal $u(t)$ with optical carrier $f_c = 193.42$ THz, as shown in Fig. 19. The corresponding in-phase and quadrature components are PAM4 sequence signals with a symbol rate 20 Gbaud and 26 bits long. Note that the in-phase and quadrature components correspond to the real $u_{\Re}(t) = a_{1\Re}(t)$ and imaginary $u_{\Im}(t) = a_{1\Im}(t)$ parts of the excitation signal $u(t)$, respectively [17]. The carrier frequency f_c is selected at the center of the passband of the Drop1 port. The crosstalk between the adjacent channels, that results from applying the 16-QAM signal to the input port of the filter, can be analyzed by performing time-domain simulation following the proposed methodology.

In a first analysis, we consider the equivalent circuit representation of Fig. 18(a), where the entire WDM filter is treated as a black box with transmission spectrum shown in Fig. 17. Such a model is computed by extracting the scattering matrix of the entire filter and by building the corresponding CVF model with 19 poles, thus achieving a maximum absolute error below -80 dB. As a reference, the time-domain simulation of the CVF model of the WDM filter is carried out by the MATLAB routine *lsim*. Then, the corresponding SPICE equivalent circuit model is constructed as explained in Section III. Such circuit model is excited and terminated in LTspice according to Section III-C. Once the corresponding SPICE simulation has finished, the forward wave a_1 at $P1$ can be recovered from the voltage and current at $P1$ and must equal the input signal $u(t)$. This is verified in Fig. 20, which demonstrates that the equivalent circuit is

correctly excited. The outputs (backward waves) at the three drop ports are plotted in Fig. 21. One can still distinguish the 4-levels of the PAM4 at port Drop1 ($P4$) despite the higher frequency components being filtered out, resulting in smoother signal transitions. The signals at ports Drop2 ($P6$) and Drop3 ($P8$) on the other hand are affected by crosstalk. Indeed, the amplitude of the time-domain signals at ports Drop2 ($P6$) and Drop3 ($P8$) increases in correspondence to the transitions of the signals at port Drop1 ($P4$). Furthermore, we can observe that the results from MATLAB and LTspice are in high agreement: the maximum absolute error for all port signals is less than 9×10^{-4}.

In the following, we compute an equivalent circuit for each DC and WG forming the filter in Fig. 16, and then connect them as discussed in Section III-C to obtain the equivalent circuit representation of the entire WDM filter, illustrated in Fig. 18(b). Hence, the CVF models of the 23 devices (9 DCs and
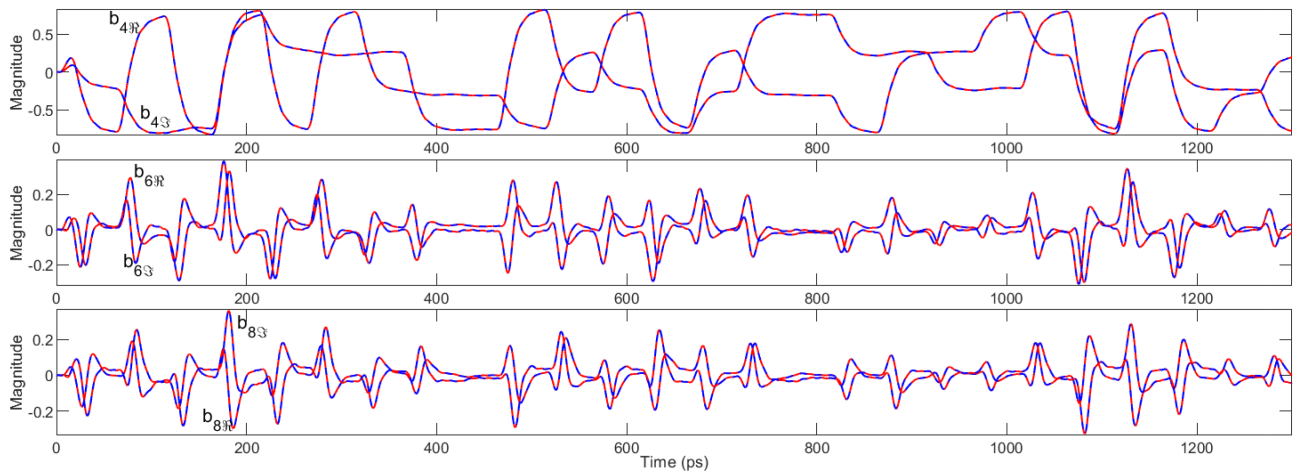
Fig. 21.   The outputs (backward waves) at the three drop ports of the WDM filter. The red lines represent the simulation results of the overall CVF model in MATLAB, while the blue dashed lines represent that of the *SPICE model of the entire WDM filter* in LTspice.

14 WGs) are constructed separately with three poles, based on their scattering matrices. The maximum absolute error between these CVF models and the corresponding scattering parameters data is smaller than -95 dB. Note that, the WDM filter under study is formed by connecting multiple instances of the same devices: for example, the directional coupler DC1 is used six times in the WDM filter (see Fig. 16). Hence, the model for the same devices must be built only once, and then it can be reused as needed.

All CVF models obtained so far can be converted into corresponding SPICE equivalent circuits via the method presented in Section III. Lastly, the 23 equivalent circuits are properly connected, according to the proposed technique in Section III-C, thereby forming the final SPICE circuit model of the WDM filter. Time-domain simulations are performed with the same settings described above, when a single SPICE equivalent model of the entire WDM circuit was computed. Simulation results agree very well with the reference results in MATLAB, as it can be seen in Fig. 22, illustrating the port signals at $P1$, $P2$, and $P5$. For clarity, only the signals at the time window from 200 ps to 800 ps are shown. Note that, the backward waves at ports $P1$ and $P5$ are the result of the counter-propagating light inside the ring resonators, and they are correctly simulated because the backscattering of the DCs in Fig. 16 is captured in Lumerical FDTD and then properly incorporated into the model by the CVF technique. Similar results can be obtained for all other port signals, thus proving that the connection method proposed in Section III is valid and accurate. More specifically, the maximum absolute error for all port signals among the reference results in MATLAB and the ones obtained by connecting SPICE models in LTspice is less than 8×10^{-3}. While the simulation results are still accurate, this error is relatively larger than the one obtained by computing an equivalent circuit starting *directly* from the scattering parameters of the entire WDM filter. Indeed, in the latter case the equivalent circuit and the state-space CVF model are mathematically the same model, but solved in different simulators (LTspice and MATLAB, respectively). Instead, when computing separate models for each component of the WDM
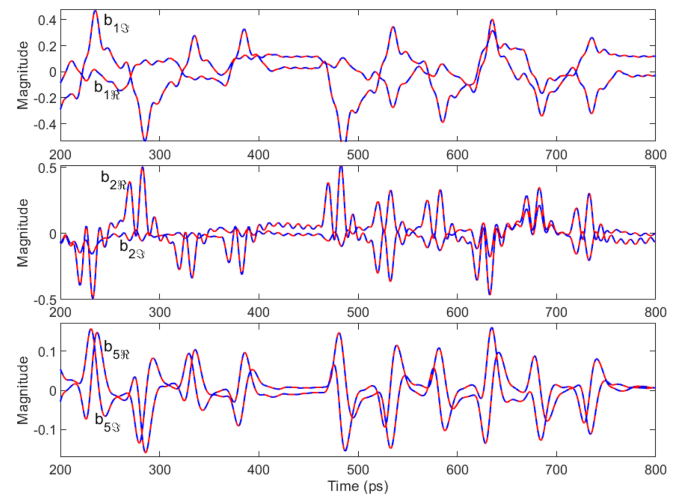

Fig. 22.   The outputs (backward waves) at $P1$, $P2$, $P5$ of the WDM filter. The red lines represent the simulation results of the overall CVF model in MATLAB, while the blue dashed lines represent the results obtained by simulating the *connected SPICE equivalent models of DCs and WGs* in LTspice.

filter, the modeling error can propagate and accumulate. Hence, it is relevant to compute accurate CVF models when connection with other circuit elements is desired.

It is important to remark that, by seperately computing an equivalent circuit for each component of the filter, not only signals at the input/output ports of the WDM filter are available to users, but also signals at each internal node of the WDM filter (e.g. signals inside the rings), which is critical for designers when carrying out system-level analyses. Indeed, Fig. 23 shows the incident waves with regard to DC2 inside the rings at Node1, Node2 and Node3 in Fig. 16. Whereas, only signals at ports $P1$ to $P8$ are available when modeling the scattering parameters of the entire WDM filter via CVF, as shown in Figs. 20 and 21. This is because CVF is a black-box modeling method: it captures the input/output behavior of the system under study, starting from its scattering parameters representation. However, it has no knowledge of the architecture of the system under study.
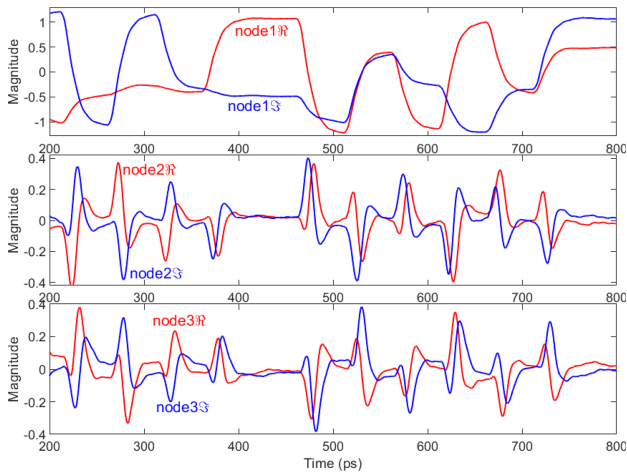
Fig. 23. The forward waves (with regard to DC2) inside the rings at Node1, Node2, Node3 of the WDM filter, obtained by simulating the *connected SPICE equivalent models of DCs and WGs* in LTspice.

TABLE I
ACCURACY AND EFFICIENCY OF THE TIME-DOMAIN SIMULATIONS WITH THE DIFFERENT WDM FILTER MODELS

Models	Accuracy (maximum absolute error)	Simulation time
Overall CVF model in MATLAB	/	0.12s
Overall SPICE model	9×10^{-4}	11.2s
Connected SPICE model	8×10^{-3}	11.3s

Indeed, in the proposed approach the equivalent circuit is built starting from the system of ordinary differential equations (6), which depends on the CVF state-space representation. Hence, voltages and currents for each component of the equivalent circuit (i.e. resistors, capacitors, controlled sources) depend on the value of the CVF state-space matrices, rather than on the physical components of the circuit. In our problem setting, this makes the port signals at all the internal nodes of the WDM filter inaccessible, unless the filter components are modeled separately.

Table I summarizes the simulation time and accuracy of the different WDM filter models. Such simulation times have been obtained using a personal computer with Intel Core i5 processor and 8 GB RAM. The reasons for the difference in computational time between MATLAB and the circuit simulator are the same as described in Section IV-B. Note that, the SPICE simulation time depends on several factors, such as number of poles in CVF models, time steps, error tolerance setting, and the duration of the simulation. Indeed, modeling wide frequency ranges and dynamic frequency responses can lead to CVF models with a relatively large number of poles. The same is true for circuits which contain long delay lines. A large number of poles will correspond to a large(r) size of the state-space model (see (2)), which translates into additional complexity of the final SPICE netlist. Additionally, small time steps are required when simulating high frequency signals, which also slows down time-domain simulations.

V. CONCLUSION

This paper presented an approach to build SPICE-compatible equivalent circuit models of passive PICs, thus enabling accurate and efficient time-domain simulations of photonic devices in standard EDA software. Since the proposed method is based on the scattering parameters representation, it is widely applicable to a large class of passive PICs and is able to capture dispersion, backscattering, and wavelength dependent effects in the circuit under study. The introduction of equivalent voltages and currents for optical waveguides allows to preserve the bi-directional nature of signals propagation in the equivalent circuit, leading to a more compact representation with respect to other techniques available in literature. The proposed method holds the potential for photonic-electronic co-simulation with time-variable active optical components (lasers, high-speed modulators, photodetectors, etc.) and high-speed electronic circuits (drivers, TIAs, control electronics, etc.) and will be further investigated in future works. Time-domain simulations of two single photonic circuits and a hierarchical photonic circuit, constructed by interconnecting many equivalent SPICE-compatible circuits, were presented to verify the feasibility and accuracy of the proposed approach.

REFERENCES

[1] W. Bogaerts and L. Chrostowski, "Silicon photonics circuit design: Methods, tools and challenges," *Laser Photon. Rev.*, vol. 12, no. 4, 2018, Art. no. 1700237.

[2] F. Bœuf, J. F. Carpentier, C. Baudot, P. Le Maitre, and J.-R. Manouvrier, *Silicon Photonics III: Systems and Applications*, 1st ed. Berlin Heidelberg, Germany, Springer, 2016, ch. 10, pp. 277–315.

[3] P. Gunupudi, T. Smy, J. Klein, and Z. J. Jakubczyk, "Self-consistent simulation of opto-electronic circuits using a modified nodal analysis formulation," *IEEE Trans. Adv. Packag.*, vol. 33, no. 4, pp. 979–993, Nov. 2010.

[4] C. Sorace-Agaskar, J. Leu, M. R. Watts, and V. Stojanovic, "Electro-optical co-simulation for integrated CMOS photonic circuits with VerilogA," *Opt. Exp.*, vol. 23, no. 21, pp. 27180–27203, Oct. 2015.

[5] M. J. Shawon and V. Saxena, "Rapid simulation of photonic integrated circuits using verilog-a compact models," *IEEE Trans. Circuits Syst. I: Reg. Papers*, vol. 67, no. 10, pp. 3331–3341, Oct. 2020.

[6] Z. Zhang et al., "Compact modeling for silicon photonic heterogeneously integrated circuits," *J. Lightw. Technol.*, vol. 35, no. 14, pp. 2973–2980, Jul. 2017.

[7] P. Qiao, G.-L. Su, Y. Rao, M. C. Wu, C. J. Chang-Hasnain, and S. L. Chuang, "Comprehensive model of 1550 nm MEMS-tunable high-contrast-grating VCSELs," *Opt. Exp.*, vol. 22, no. 7, pp. 8541–8555, Apr. 2014.

[8] H. Štimac, R. Blečić, R. Gillon, and A. Barić, "Differential electro-optical equivalent circuit model of a vertical-cavity surface-emitting laser for common-mode rejection ratio estimation," *J. Lightw. Technol.*, vol. 37, no. 24, pp. 6183–6192, Oct. 2019.

[9] M. Shekarpour and M. H. Yavari, "An equivalent circuit model of passively mode-locked hybrid silicon laser," *IEEE Photon. Technol. Lett.*, vol. 34, no. 11, pp. 595–598, Jun. 2022.

[10] B. Wang et al., "A compact Verilog-A model of silicon carrier-injection ring modulators for optical interconnect transceiver circuit design," *J. Lightw. Technol.*, vol. 34, no. 12, pp. 2996–3005, Jun. 2016.

[11] S. Tanaka, T. Usuki, and Y. Tanaka, "Accurate SPICE model of forward-biased silicon PIN Mach–Zehnder modulator for an energy-efficient multilevel transmitter," *J. Lightw. Technol.*, vol. 36, no. 10, pp. 1959–1969, May 2018.

[12] M. Kim et al., "Large-signal SPICE model for depletion-type silicon ring modulators," *Photon. Res.*, vol. 7, no. 9, pp. 948–954, Sep. 2019.

[13] M. Jalali, M. K. Moravvej-Farshi, S. Masudy-Panah, and A. Nabavi, "An equivalent lumped circuit model for thin avalanche photodiodes with nonuniform electric field profile," *J. Lightw. Technol.*, vol. 28, no. 23, pp. 3395–3402, Dec. 2010.

[14] D. Dai, M. Piels, and J. E. Bowers, "Monolithic germanium/silicon photodetectors with decoupled structures: Resonant APDs and UTC photodiodes," *IEEE J. Sel. Topics Quantum Electron.*, vol. 20, no. 6, pp. 43–56, Nov./Dec. 2014.

[15] J.-M. Lee, S.-H. Cho, and W.-Y. Choi, "An equivalent circuit model for a Ge waveguide photodetector on Si," *IEEE Photon. Technol. Lett.*, vol. 28, no. 21, pp. 2435–2438, Nov. 2016.

[16] X. Chen et al., "A comprehensive electro-optical model for silicon photonic switches," in *Proc. IEEE Comput. Soc. Annu. Symp.*, Hong Kong, China, 2018, pp. 76–81.

[17] Y. Ye, D. Spina, D. Deschrijver, W. Bogaerts, and T. Dhaene, "Time-domain compact macromodeling of linear photonic circuits via complex vector fitting," *Photon. Res.*, vol. 7, no. 7, pp. 771–782, Jul. 2019.

[18] A. Farsaei et al., "A novel and scalable design methodology for the simulation of photonic integrated circuits," in *Proc. Adv. Photon. Novel Opt. Mater. Appl.*, 2016, Paper no. JTu4A.2.

[19] Y. Ye, D. Spina, W. Bogaerts, and T. Dhaene, "Baseband macromodeling of linear photonic circuits for time-domain simulations," *J. Lightw. Technol.*, vol. 37, no. 4, pp. 1364–1373, Feb. 2019.

[20] D. Spina, Y. Ye, D. Deschrijver, W. Bogaerts, and T. Dhaene, "Complex vector fitting toolbox: A software package for the modelling and simulation of general linear and passive baseband systems," *Electron. Lett.*, vol. 57, no. 10, pp. 404–406, May 2021.

[21] T. Smy and P. Gunupudi, "Robust simulation of opto-electronic systems by alternating complex envelope representations," *IEEE Trans. Comput.-Aided Des. Integr. Circuits Syst.*, vol. 31, no. 7, pp. 1139–1143, Jul. 2012.

[22] D. Hamill, "Learning about chaotic circuits with SPICE," *IEEE Trans. Educ.*, vol. 36, no. 1, pp. 28–35, Feb. 1993.

[23] J. Pelloux-Prayer and F. Moradi, "Compact model of all-optical-switching magnetic elements," *IEEE Trans. Electron Devices*, vol. 67, no. 7, pp. 2960–2965, Jul. 2020.

[24] B. Gys et al., "Circuit model for the efficient co-simulation of spin qubits and their control & readout circuitry," in *Proc. IEEE 47th Eur. Solid State Circuits Conf.*, Grenoble, France, 2021, pp. 63–66.

[25] R. Neumayer, F. Haslinger, A. Stelzer, and R. Weigel, "Synthesis of SPICE-compatible broadband electrical models from n-port scattering parameter data," in *Proc. IEEE Int. Symp. Electromagn. Compat.*, Minneapolis, MN, USA, 2002, pp. 469–474.

[26] R. E. Collin, *Foundations for Microwave Engineering*, 2nd ed. Hoboken, NJ, USA: Wiley, 2001, ch. 4, pp. 220–302.

[27] K.-W. Yeom, *Microwave Circuit Design: A Practical Approach Using ADS*. New York, NY, USA: Prentice-Hall, 2015.

[28] H. Deng and W. Bogaerts, "Pure phase modulation based on a silicon plasma dispersion modulator," *Opt. Exp.*, vol. 27, no. 19, Sep. 2019, Art. no. 27191.

[29] Y. Ye, D. Spina, Y. Xing, W. Bogaerts, and T. Dhaene, "Numerical modeling of linear photonic system for accurate and efficient time-domain simulations," *Photon. Res.*, vol. 6, no. 6, pp. 560–573, Jun. 2018.

[30] A. Vladimirescu, *The Spice Book*, 1st ed. Hoboken, NJ, USA Wiley, 1994, ch. 9, pp. 278–318.

[31] K. Sou and O. L. D. Weck, "Fast time-domain simulation for large-order linear time-invariant state space systems," *Int. J. Numer. Methods Eng.*, vol. 63, no. 5, pp. 681–708, Mar. 2005.

Thijs Ullrick (Student Member, IEEE) received the M.S. degree *(cum laude)* in electronics engineering in 2008, from the Ghent University, Ghent, Belgium, where he is currently working towards the Ph.D. degree with the Department of Information Technology. He was with the Space Instrument Department of the Company OIP Sensor Systems, Oudenaarde, Belgium, from 2018 to 2020. His research interests include modeling and simulation, photonic circuit design, microwave engineering, and machine learning.

Wim Bogaerts (Fellow, IEEE) received the Ph.D. in the modelling, design and fabrication of silicon nanophotonic components from Ghent University, Ghent, Belgium, in 2004. He is currently the Professor with Photonics Research Group, Ghent University - imec, Ghent, Belgium. During this work, he started the first silicon photonics process on imec's 200 mm pilot line, which formed the basis of the multi-project-wafer service ePIXfab. In 2014, he Co-founded Luceda Photonics, spin-off company of Ghent University, IMEC, Leuven, Belgium, and the University of Brussels, Brussels, Belgium. Luceda Photonics develops unique software solutions for silicon photonics design, using the IPKISS design framework. Since 2016, he was Full-time Professor Ghent University, looking into novel topologies for large-scale programmable photonic circuits, supported by a consolidator grant of the European Research Council. His research interests include the challenges for large-scale silicon photonics: Design methodologies and controllability of complex photonic circuits, telecommunications, information technology and applied sciences. He is the Senior Member of OSA and SPIE.

Tom Dhaene (Senior Member, IEEE) received the Ph.D. degree in electrotechnical engineering from Ghent University, Ghent, Belgium, in 1993. He was a Research Assistant with the Department of Information Technology, University of Ghent, Ghent, Belgium, from 1989 to 1993. In 1993, he joined the Electronic Design Automation Company Alphabit (now part of Agilent), Santa Clara, CA, USA. He was one of the key developers of the planar EM simulator ADS Momentum. In September 2000, he joined the Department of Mathematics and Computer Science, University of Antwerp, Antwerp, Belgium, as the Professor. Since October 2007, he has been a Full Professor with the Department of Information Technology, Ghent University. He is the author or co-author of more than 250 peer reviewed papers and abstracts in international conference proceedings, journals, and books. He holds five U.S. patents.

Yinghao Ye (Member, IEEE) received the M.S. degree in electronic engineering from the Xidian University, Xi'an, China, in 2014, and the Ph.D. degree in electrical engineering from the Ghent University, Ghent, Belgium, in 2019. He was with Huawei, Shenzhen, China, from 2019 to 2020. Since 2020, he has been an Associate Professor with the Faculty of Big Data and Information Engineering, Guizhou University, Guiyang, China. His research interests include modeling and uncertainty quantification of electronic and photonic integrated circuits.

Domenico Spina (Member, IEEE) received the M.S. degree *(cum laude)* in electronics engineering from the University of L'Aquila, L'Aquila, Italy, in 2010, and the joint Ph.D. degree in electrical engineering from the Ghent University, Ghent, Belgium, and the University of L'Aquila in 2014. Since 2015, he has been a Postdoctoral Researcher with the Department of Information Technology, Ghent University. His research interests include modeling and simulation, system identification, microwave engineering, sensitivity, and uncertainty analysis.